

## Flow Mechanisms induced by Non-Axisymmetric Casing Treatment in a Transonic Axial Compressor

G. Legras<sup>1</sup>, L. Castillon<sup>2</sup>, I. Trébinjac<sup>1</sup> and N. Gourdain<sup>3</sup>

**1** LMFA, UMR 5509  
Ecole Centrale de Lyon / UCB  
Lyon 1 / INSA,  
69134, Ecully; France  
legras@cerfacs.fr  
isabelle.trebinjac@ec-lyon.fr

**2** ONERA,  
Applied Aerodynamics Department,  
92190, Meudon, France  
lionel.castillon@onera.fr

**3** CERFACS, CFD-Team,  
31057, Toulouse, France  
gourdain@cerfacs.fr

### Abstract

Passive control devices based on casing treatments have already shown their capability to improve the flow stability in axial compressors. Among many geometries that have been investigated, non-axisymmetric slots show a good ability to enhance stall margin. However their optimization remains complex due to a partial understanding of the related flow mechanisms. The present paper proposes to numerically investigate a transonic axial compressor rotor that incorporates a slot-type casing treatment. Numerical unsteady flow simulations are performed using an unsteady overset grids method and a phase-lagged approach. Numerical results obtained with and without casing treatment are compared and validated with experimental data. In order to quantitatively assess the interaction mechanisms between slots and the near casing flow, a budget analysis of the unsteady axial momentum equation is performed on a control volume located in the rotor tip region. Results show that flow reinjection of the slots provides additional net axial force due to axial transport of axial momentum on the near casing flow. This flow energizing mechanism is assumed to be responsible for the stability enhancement induced by non-axisymmetric casing treatments.

**Keywords:** Transonic axial compressor, casing treatment, non-axisymmetric casing slots, tip leakage flow.

### Introduction

Today, it is mandatory for compressor designers to improve performance in terms of efficiency and operating range characterized by the stall margin at low mass flow rate. One of the main difficulties encountered in this process is that compressor stall is not always controlled through normal aerodynamic design. Thus stall prevention techniques must be used and one promising technology known to bring substantial stability for tip-critical compressor rotor is Casing Treatment (CT) (Greitzer et al.<sup>[1]</sup>). This passive control device consists of slots within the rotor casing and presents various types of geometries: circumferential grooves, non-axisymmetric slot-type CT and self-recirculating flow channels, honeycomb.... Hathaway<sup>[2]</sup> provides an extensive overview of the research studies over the last 50 years that attempt to uncover the physics behind the improvement in stall margin.

Among the geometries that have been investigated, non-axisymmetric slots exhibit the ability to enhance the stall margin (Wilke and Kau<sup>[3]</sup>, Lin et al.<sup>[4]</sup>, Ning et al.<sup>[5]</sup>). An important aspect of this kind of CT is flow

recirculation through the slots from the rear of the passage to the front and driven by the mean pressure rise of the compressor. This process is similar to a mechanism of bleeding critical blockage zones out of the blade passage and upstream reinjection. This kind of geometry improves the flow condition near the blade tip by repositioning the tip clearance vortex further towards the trailing edge of the blade passage and delaying the forward movement of tip leakage vortex (Lu et al.<sup>[6]</sup>). The effect of reinjection is apparently relevant but their optimization remains complex due to a partial understanding of the related physical mechanisms.

Previous works have been done to find a methodology that provides further insight into CT flow mechanisms. Shabbir and Adamczyk<sup>[7]</sup> firstly proposed an approach based on a budget analysis of the steady axial momentum equation close to the rotor casing. However, their methodology is restricted to the understanding of steady flow mechanisms and to the application on configuration with circumferential CT. Legras et al.<sup>[8-9]</sup> proposed a generalization of the Shabbir and Adamczyk<sup>[7]</sup> approach that aims at further understanding flow mechanisms and

quantitatively diagnosing 3D complex flows like those induced by any kind of CT geometries. This Extended Model (EM) calculates the budget analysis of the Navier-Stokes set of unsteady equations and has been successfully applied in previous works. Analysis of steady axial and radial momentum equations has been performed to investigate NASA Rotor 37 with circumferential CT by Legras et al.<sup>[8]</sup>. Furthermore, analysis of the unsteady axial momentum equation has been retained to investigate the unsteady influence of upstream stator wakes on circumferential CT mechanisms (Legras et al.<sup>[9]</sup>). In fact, results reveal that the EM turns out to be useful to ascertain CT efficiency and to provide guidance for groove design.

## Compressor model

The single stage transonic compressor test rig in School of Jet Propulsion, Beijing University of Aeronautics & Astronautics is retained for the present numerical investigation (Fig. 1). A brief description of the test rotor can be seen in Table 1. In the experiment, the stator is placed far downstream of test rotor, thus the isolated rotor environment can be established. Experimental and numerical studies of the test case can be found in Lin et al.<sup>[4]</sup> and Ning et al.<sup>[5]</sup>.

1. Inlet plane; one total pressure comb
2. Outlet plane I; one fast response pressure probe, monitoring the onset of rotating stall.
3. Outlet plane II; two total pressure combs

**Table 1 Description of the test rotor (Lin et al.<sup>[4]</sup>)**

### Design of the slot-type casing treatment

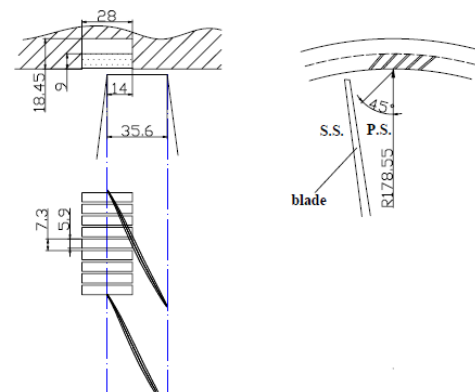


**Fig. 2 Sketch of the slot-type casing treatment (Lin et al.<sup>[4]</sup>)**

passage and one CT slot. The physical time step is chosen so that 1530 and 170 iterations are set to solve respectively the blade passing period in the CT frame and the slot passing period in the rotor frame of reference. The two-equation model proposed by Wilcox<sup>[13]</sup> based on a  $k-\omega$  formulation was used to model turbulence. The flow is assumed to be fully turbulent since the mean Reynolds number based on the blade chord is approximately  $5.10^6$ .

Concerning the boundary conditions, a spatial periodicity is applied on the lateral faces of the blade passage. The overset grid boundary conditions are coupled with a phase-lagged condition at the interface between rotor and slot. At the lateral faces of the recess chamber, a phase-lagged boundary condition is used. At solid boundaries, an adiabatic wall condition is imposed. An axial injection boundary condition is applied upstream and a throttle condition coupled with a simplified radial equilibrium is used downstream. Stage throttling is modified by imposing a static pressure downstream the rotor with respect to a reference level of static pressure.

### Meshing strategy

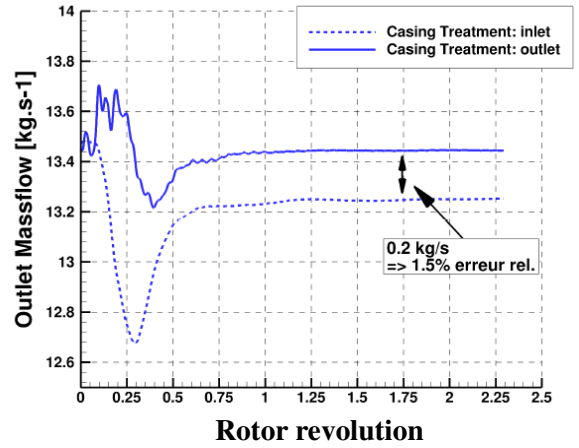
The SW configuration is discretized with a low Reynolds multi-block-structured approach using an “O4H” meshing strategy. The typical dimensions of a blade passage mesh are 161, 89 and 169 points respectively in the axial, radial and tangential directions. The tip leakage region is discretized using “OH” grid topology with 25 points in the radial direction. The meshes are clustered towards the solid boundaries in order to reach the resolution requirement of  $y^+ \approx 1$  (the size of the first layer is approximately  $1 \mu m$ ). For the SW case, this meshing strategy leads to a total nodes number of 2.7 millions points.

The mesh used for the CT configuration is based on the SW mesh at which Chimera blocks modelling one slot have been added. One unique slot is meshed using two H blocks. The dimensions of a treatment vane are 61, 37 and 59 points respectively in the axial, radial and tangential directions, whereas dimensions of the recess chamber mesh are 61, 67 and 41 respectively. The total grid point of the case with CT is approximately 3 millions points.

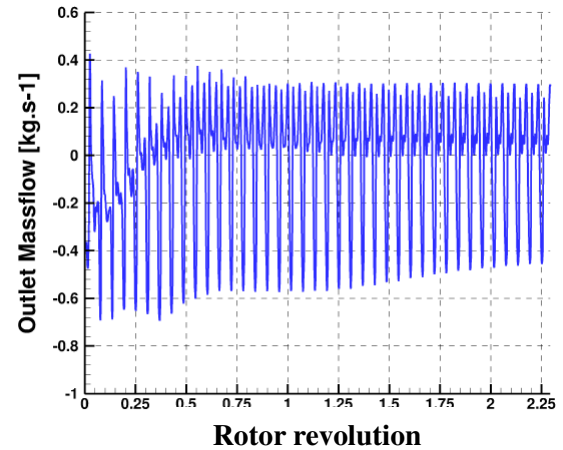
### Results and Discussion

Before discussing on the overall performance and the physical analysis, it is instructive to comment on the history of the mass flow rates through the blade passage and at the slot entrance. Fig. 3 shows curves obtained from a CT calculation at peak efficiency of design speed. It is seen that the blade passage reaches “a quasi steady state solution” (Fig. 3.a.), whereas at slot openings the mass flow rate is clearly unsteady (Fig. 3.b.). These results have been already observed by Lin et al.<sup>[4]</sup> and Ning et al.<sup>[5]</sup>, who explained this phenomenon by the large number of slots of one order of magnitude higher than the number of rotor blades. Indeed, the unsteady

time scale of one slot is small compared to that of the blade passage, thus the unsteadiness of blade passage is weak. Two rotor revolutions are needed to reach a periodic state.



a) Inlet and outlet mass flow rates through the blade passage



b) Mass flow exchanged between blade passage and one slot

Fig. 3 Mass flow convergence histories of the CT configuration at peak efficiency point.

### Overall performance

Rotor characteristics of both SW and CT configurations obtained at 98% speed by the experiment (Lin et al.<sup>[4]</sup>) and predicted by unsteady simulations are compared in Fig. 4. The numerical curves shapes are in fairly good agreement with the measurements. However, numerical characteristics are shifted due to a larger mass flow rate at choked conditions than the measured value (as predicted by Lin et al.<sup>[4]</sup> and Ning et al.<sup>[5]</sup>). Simulations overestimate total pressure as well as efficiency magnitudes. The stable operating range of the SW configuration is correctly predicted. Concerning CT case, simulations clearly underestimate the operating range due to the onset of stall point at higher mass flow rate than the experiment. Finally, the calculated efficiency curves of the CT configuration show lower magnitude

than the SW case one in the SW operating range, whereas the magnitude of the total pressure CT curve is similar. These differences have also been observed by other authors who numerically investigated the present test case (Lin et al.<sup>[4]</sup>, Ning et al.<sup>[5]</sup>). Therefore, it was considered that the numerical model is able to reveal the overall flow mechanisms occurring near the outer casing, which is essential for the objective of the present work aiming at understanding the local influence of CT slots.

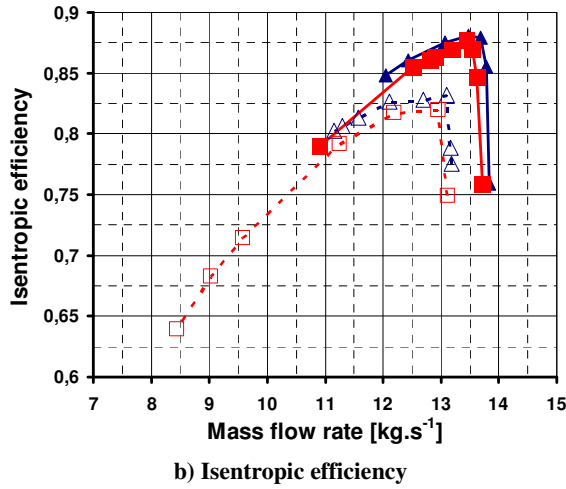
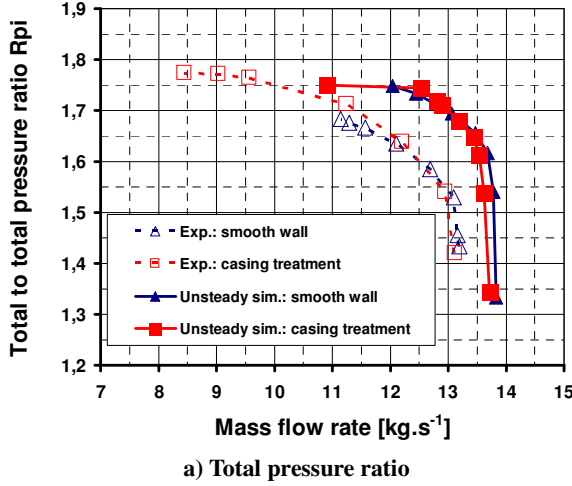


Fig. 4 Experimental and numerical characteristics of the SW and CT rotor configurations at design speed.

#### Tip flow mechanisms of the SW configuration near stall operating point

Fig. 5 and Fig. 6 show respectively the relative helicity  $H (= \vec{W} \cdot \vec{r} \otimes \vec{t} \vec{W})$  and the relative total pressure flow field with isolines of relative Mach number at blade tip ( $h/H=97.5\%$ ) for the simulated SW and CT configurations. These plots present the time-averaged results obtained at the SW near stall operating point. The helicity variable helps on revealing vortices, whereas relative total pressure highlights high losses regions.

SW results (Fig. 5.a) show a conventional rotor tip flow topology that develops in axial transonic compressor. The pressure difference between pressure and suction sides at the blade tip gap leads to the onset of a tip leakage flow. It rolls-up into a streamwise vortex that develops close to the leading edge on the blade suction side. The vortex is then carried out in the channel toward the pressure side of the adjacent blade until it interacts with the blade passage shock at midway between pressure and suction sides of two adjacent blades. The vortex core structure expands downstream of the shock wave (Fig. 6.a.). This change leads to a large blockage effect that deflects the main flow toward the neighbouring channel, marking the last stable numerical operating point. Further downstream in the channel, a coherent structure remains, which continues its path until it impacts the pressure side of the adjacent blade at approximately  $x/C=40\%$ . Moreover, the detached shock impinges on the suction side of the adjacent blade at approximately  $x/C=50\%$ .

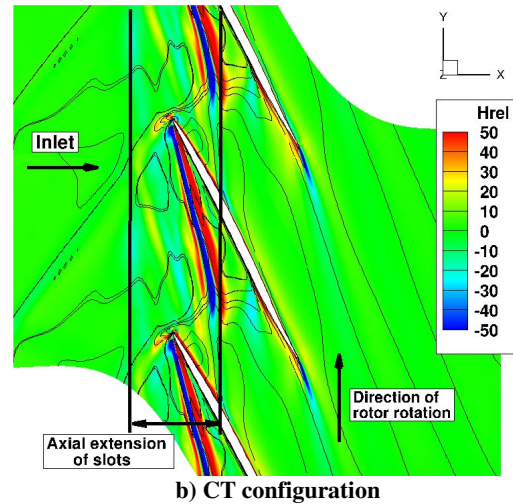
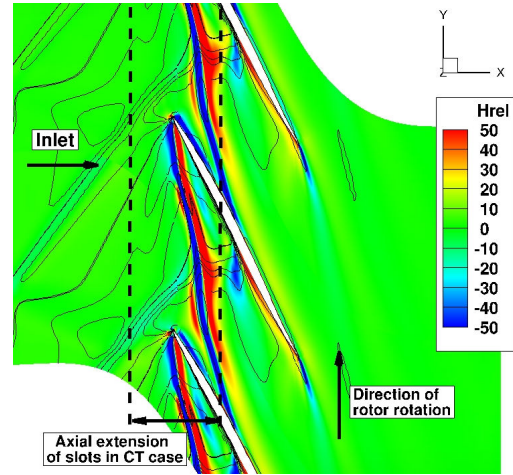
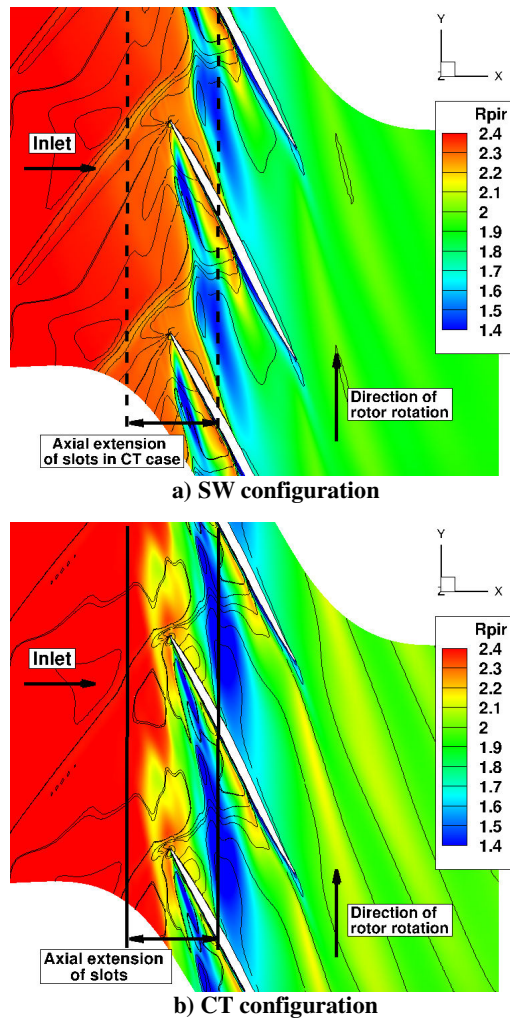


Fig. 5 Time-averaged maps of relative helicity with relative Mach number contours at  $h/H=97.5\%$  for the SW near stall operating point.





**Fig. 6 Time-averaged maps of relative total pressure with relative Mach number isolines at  $h/H=97.5\%$  for the SW near stall operating point.**

#### Slot-type CT flow mechanisms

Numerical results of the CT configuration (Fig. 5.b) highlight the same vortex topology than SW case but differ in two facts. First, it can be observed a lower trajectory angle of the tip leakage vortex relative to the blade's chord of approximately  $2^\circ$ . In fact, CT slots attenuate the spread of the tip leakage vortex perpendicular to the blade due to a lower blade loading at tip than SW case (results not shown). Since the stall inception is usually associated with the tip clearance vortex moving upstream, this CT effect on the tip flow is assumed to be the main mechanism that explains the delay of the stall at lower mass flow rate than the SW configuration. Secondly, the region of helicity deficit (Fig. 5.b) and low total pressure (Fig. 6.b.) downstream the shock suggests that the tip leakage vortex/shock interaction is much stronger than in the SW case. It explains the slightly loss in efficiency seen in Fig. 4.b.

These changes of the rotor blade tip flow properties are mainly due to the important fluid exchanges that occur between the slots and the blade channel (already

shown in Fig. 3.b.). In order to visualize this complex interaction, Fig. 7 illustrates at SW near stall operating point one instantaneous contour plot of relative Mach number at blade tip ( $h/H=97.5\%$ ) with radial velocity normalized by tip rotor speed ( $V_r/U_{tip}$ ) at the 9 slots entrance. Since the flow in the blade channel is almost a “quasi-steady flow”, it is believed that the relevant flow mechanisms can be deduced from the information taken at one instant. In fact, flow fields taken at other instants (not shown in the paper) present the same global flow mechanisms, in agreement with results obtained by Ning et al.<sup>[5]</sup>.

Based on results shown in Fig. 7, regions of bleed and injected fluid by CT slots can be clearly identified. In the frame of reference relative to the rotor, it can be observed three main regions of high pressure where flow is bled by the rear part of the CT slots: (i) near the blade pressure side, (ii) near the suction side just downstream the blade passage shock and (iii) over the flow blockage associated with the tip leakage vortex/shock interaction. Similarly, areas of reinjection flow are located just in front of the blade passage shock and mainly concern the middle part of the CT slots. One can notice that the first third part of the cavities does not participate to the flow exchange with the through-flow stream, except for two slots located at midway between pressure and suction sides of two adjacent blades.

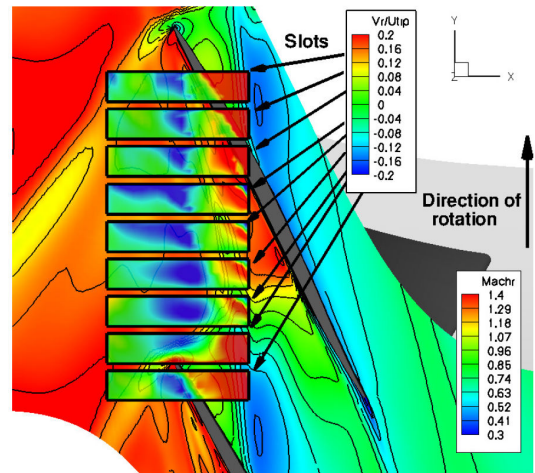


**Fig. 7 Instantaneous map of  $V_r/U_{tip}$  at slot entrance with relative Mach number distribution at  $h/H=97.5\%$  of the CT configuration at SW near stall point.**

#### Flow Mechanisms Analysis with the EM

##### Analyzed equation and numerical resolution

In order to get further insight into the mechanisms of interaction between rotor and CT slots, the EM model is used to analyze the balance of the unsteady axial momentum equation in the rotor tip clearance. This equation is chosen since it describes the global flow behavior across the rotor channel, specially its pressure rise. The description of the EM and its application on steady and unsteady flow problems are fully described in

Legras et al.<sup>[8-9]</sup>. To summarize, the EM principle relies on the determination of the fluxes balances of each term of the Navier-Stokes equations (finite volume formulation) based on numerical CFD results on structured meshes. Therefore, the equation considered by the EM can be expressed as follows:

$$\begin{aligned} & \sum_{r,\theta,z} \Delta(\rho W_z W_r A_r) + \sum_{r,\theta,z} \Delta(\rho W_z W_\theta A_\theta) + \sum_{r,\theta,z} \Delta(\rho W_z^2 A_z) + \sum_{r,\theta,z} \Delta(P_s A_z) \\ & \sum_{r,\theta,z} \Delta(F_{\lambda 2}) + \sum_{r,\theta,z} \Delta(F_{\lambda 4}) - \sum_{r,\theta,z} \Delta(\tau_{rz} A_r) - \sum_{r,\theta,z} \Delta(\tau_{z\theta} A_\theta) - \sum_{r,\theta,z} \Delta(\tau_{zz} A_z) \\ & = R(\rho W_z) = -V \frac{\partial \rho W_z}{\partial t} \end{aligned} \quad (1)$$

where  $A_{r,\theta,z}$  and  $V$  correspond respectively to the projection areas and the volume of the control domain,  $\rho$  the density,  $P_s$  the static pressure,  $W_{r,\theta,z}$  the components of the relative velocity,  $\tau_{rz,\theta,z}$  the components of the sum of viscous and turbulence stress tensors,  $F_{\lambda 2}$  and  $F_{\lambda 4}$  respectively the 2<sup>nd</sup> and 4<sup>th</sup> numerical scalar artificial dissipation fluxes (these have been added to the equation due to the use of 2<sup>nd</sup>-order centered space-discretization scheme of Jameson<sup>[12]</sup> in the numerical simulations).  $R(\rho W_z)$  is the numerical modelling residual of variable  $\rho W_z$  and also corresponds to the opposite of the time derivative term  $\partial(\rho W_z)/\partial t$ . The operator  $\Delta()$  is introduced to characterize the fluxes balance on an individual hexahedral cell, whereas operator  $\Sigma()$  performs the cumulative sum on each grid cell constitutive of the fluid control volume.

#### Definition of the fluid control volume

The control volume illustrated in Fig. 8 surrounds the rotor tip clearance. It is circumferentially delimited by the rotor blade pitch, axially extended upstream and downstream of the rotor blade tip, and radially bounded between the 5<sup>th</sup> and the 20<sup>th</sup> grid layers in the tip clearance (total: 25).

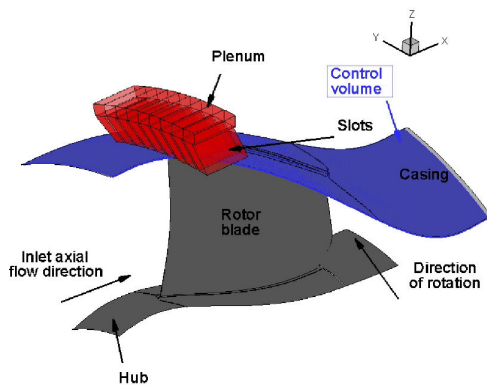


**Fig. 8 View of the test case configuration and the control volume used for the budget analysis of the unsteady axial momentum equation.**

#### Global flow mechanisms

Instantaneous axial momentum balances, for both SW and CT cases at SW near stall point, are obtained for 17

instants equally spread over one CT slot passing temporal period ( $T_{CT}$ ). The time-averaged budgets of the axial momentum equation are shown as histograms in Fig. 9. This kind of representation provides a macroscopic view of the forces acting on the control volume illustrated in Fig. 8.

Before discussing on the physical analysis, it is instructive to comment on the magnitude of the numerical terms of the time-averaged balances. The time-averaged temporal derivative term  $\partial(\rho W_z)/\partial t$  converges to zero supporting that the calculations correctly reach a time-periodic state. Moreover, it can be observed that scalar artificial viscosity fluxes ( $F_{\lambda 2}$  and  $F_{\lambda 4}$ ) are insignificant.

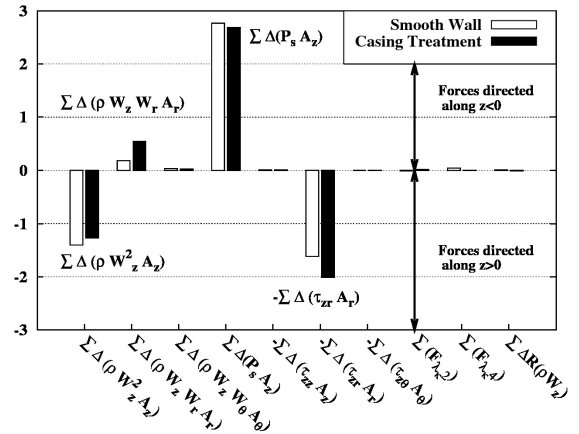


**Fig. 9 Time-averaged budgets of the axial momentum equation applied on respectively on the SW and CT control volumes (Fig. 8) at SW near stall point.**

#### SW configuration

SW results in Fig. 9 highlight the presence of four main net axial forces being applied on the control volume. Two different groups of forces can be distinguished. The first one counts forces acting in opposite direction of the flow ( $z<0$ ):

- the axial pressure force  $\Sigma\Delta(P_s A_z)$  (i.e. the flow pressure rises across the rotor) for  $\approx 93\%$ ;
- the net axial force due to the transport of the axial momentum across the radial faces  $\Sigma\Delta(\rho W_z W_r A_r)$  for  $\approx 7\%$ . This term is very weak due to  $W_r \sim 0$  imposed by the cylindrical shape annulus.

The second group includes the forces acting along the flow advance direction ( $z>0$ ) and counts:

- the net axial force due to the transport of the axial momentum across the longitudinal faces  $\Sigma\Delta(\rho W_z^2 A_z)$  for  $\approx 45\%$ ;
- the net axial shear force on the radial faces of the control volumes  $-\Sigma\Delta(\tau_{rz} A_r)$  for  $\approx 55\%$ . This term is created by casing and blade tip boundary layers or tip leakage flow.

All other terms are zero due to periodicity or to the radial thickness of the control volume.

It is worth noticing that the forces applied on the near casing flow correspond, except in magnitudes, to those

observed in similar works done by Shabbir and Adamczyk<sup>[7]</sup> and Legras et al.<sup>[8-9]</sup>. Moreover, cross comparisons of the current SW results with the previous studies can be done in terms of flow regime influence (subsonic vs. transonic flow), and impact of the annulus shape (cylindrical vs. conical). Although the present test case is a transonic compressor, the axial momentum balance shows lower values of convective forces than the transonic test case NASA Rotor 37 (Legras et al.<sup>[8]</sup>). A conclusion about this last test case indicates that strong convective forces are induced by the conical shape annulus. The casing imposes a radial velocity  $W_r$  component to the near casing flow, thus creating radial transport of axial momentum  $\sum \Delta(\rho W_z W_r A_r)$  acting in opposite direction to the flow advance (i.e.  $z < 0$ ). Thereby, the low value of  $\sum \Delta(\rho W_z W_r A_r)$  in Fig. 9 proves that the shape of the current rotor casing has a greater influence than the flow regime. This observation is further confirmed by comparison with budget analysis done in tip clearance of subsonic with cylindrical casing compressor rotors (see Shabbir and Adamczyk<sup>[7]</sup>, Legras et al.<sup>[9]</sup>). In fact, axial momentum budget for cylindrical shape annulus shows similar trend whether the regime is subsonic or transonic (characterized by low value of  $\sum \Delta(\rho W_z W_r A_r)$  and a strong pressure gradient  $\sum \Delta(P_s A_z)$ ).

#### CT configuration

CT results in Fig. 9 reveal the same type of forces acting on the blade tip flow than SW case but with different magnitudes. One can observe that the total forces directed along  $z < 0$  (as well as forces directed along  $z > 0$ ) has increased by approximately 12% compared to SW case.

The magnitude of pressure rise across the rotor  $\sum \Delta(P_s A_z)$  is maintained in agreement with the predicted overall performances (Fig. 4) but accounts now for approximately  $\approx 83\%$  of the total force directed along  $z < 0$ , whereas the force  $\sum \Delta(\rho W_z W_r A_r)$  accounts for  $\approx 17\%$ . This observation suggests that the fluid exchanges between the CT slots and the rotor channel, characterized by the radial velocity magnitude  $W_r$  (Fig. 7), contributes to additional force to balance the axial momentum equation and blocks the advance of the main passage flow.

Concerning forces acting along the main flow direction ( $z > 0$ ), the magnitude of the force  $\Delta(\rho W_z^2 A_z)$  has slightly decreased compared to SW case and accounts for  $\approx 38\%$ . However, the main change occurs for the axial viscous force  $-\sum \Delta(\tau_{rz} A_r)$  that accounts for  $\approx 60\%$  and has increased by approximately 18% compared to SW case. This observation can be relied to the slightly loss in efficiency observed in Fig. 4.

#### Unsteady flow mechanisms

Fig. 10 presents the temporal evolution, over the CT slot passing temporal period  $T_{CT}$ , of the main terms involved in the unsteady axial momentum equation for both SW and CT configurations. This analysis allows us

to gain a quantitative and qualitative knowledge of the contribution of the time derivative term  $\partial(\rho W_z)/\partial t$ .

Plots in Fig. 10 indicate that all terms present a “quasi-steady” behaviour, supporting that unsteadiness of the CT interaction with the through flow stream is insignificant. This observation is especially confirmed by the zero magnitude over  $T_{CT}$  of the time derivative term  $\partial(\rho W_z)/\partial t$ . This result is not surprising since it was announced by the previous mass flow convergence histories through the rotor channel (Fig. 3.a.). Despite the high temporal resolution of the CT slot passing temporal period ( $T_{CT} = 170$  iterations), this particular test case fails to meet expectations in term of analysis of unsteady flow interaction between the CT slots and the rotor channel. However, the effort is now focused on the analysis of local changes of the axial momentum balance in order to get more qualitative and quantitative information on the contribution of the CT slots.

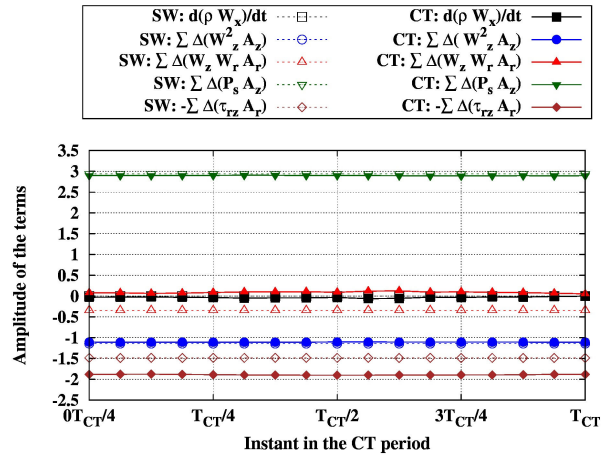


Fig. 10 Temporal evolution of the main terms of the unsteady axial momentum equation for the SW and CT configuration.

#### Axial evolution of the time-averaged axial forces

The cumulative sums along the axial direction of the time-averaged terms  $-\sum \Delta(\tau_{rz} A_r)$ ,  $\sum \Delta(\rho W_z W_r A_r)$  and  $\sum \Delta(\rho W_z^2 A_z)$  previously shown in Fig. 9 are presented in Fig. 11. Results are plotted for both SW and CT configurations. These diagrams provide information on the regions where flow is highly constrained and also on CT contribution. The shaded band denotes the axial location of the slots. In order to rely these curves to the flow physics, Fig. 12, Fig. 13 and Fig. 14 show respectively at mid-gap the flow fields of  $-\Delta(\tau_{rz} A_r)$ ,  $\Delta(\rho W_z^2 A_z)$  and  $\Delta(\rho W_z W_r A_r)$  at cell center.

#### SW configuration

Results in Fig. 11.a. of the SW configuration show that the efforts evolve in amplitude along the axial direction in a nonlinear manner.

The curve of viscous term  $-\sum \Delta(\tau_{rz} A_r)$  begins to grow at approximately  $x/C=10\%$  and can be relied to the



growing expansion of the tip leakage vortex (region A in Fig. 12.a.).

Curve of the term  $\sum \Delta(\rho W_z^2 A_z)$  presents negative value before the blade leading edge due to the detached shock as illustrated by Fig. 13.a. Further downstream in the blade channel, the curve abruptly evolves at  $x/C \approx 40\%$  and then increases in negative values. According to Fig. 13.a., this region of abrupt change relies on the complex interaction of the tip leakage flow with the blade passage shock.

Concerning the axial force  $\sum \Delta(\rho W_z W_r A_r)$ , the curve axially evolves in “quasi” opposite magnitude of  $\sum \Delta(\rho W_z^2 A_z)$  curve. As observed by Legras et al.<sup>[9]</sup>,  $W_r$  acts here as a “coefficient of amplification”. This observation is confirmed by Fig. 14.a. where contours plots are very similar to those of  $\sum \Delta(\rho W_z^2 A_z)$  in Fig. 13.a.

To resume, the SW result highlights strong axial force magnitude due to the tip leakage flow, the detached blade shock and the interaction between leakage flow and blade passage shock.

#### CT configuration

Results in Fig. 11.a. of the CT configuration clearly highlight the local contribution of the slots.

The curve shape of the viscous term  $-\sum \Delta(\tau_{rz} A_r)$  are very similar to those of the SW case, except that the growth rate begins at approximately  $x/C = 20\%$ . Since this term can be relied to the tip leakage flow, this result can be explained by the attenuation of the spread of the leakage flow perpendicular to the blade. This observation has been previously observed in Fig. 5.b. and is confirmed in Fig. 12.b., where the tip leakage flow (blue region A) expansion is attenuated by CT slots and the viscous effort is reduced compared to SW case. However, referring to the histograms in Fig. 9, CT configuration shows higher magnitude of viscous term  $-\sum \Delta(\tau_{rz} A_r)$ . In fact, contour plots in Fig. 12.b. indicate the presence of a second region of high viscous axial force denoted B and located along the rear part of the CT slots. This result suggests that the flow bleeding mechanism induces strong shear layer that can increase viscous losses. Furthermore, it can explain the efficiency losses observed with the use of slot-type CT.

CT curve of  $\sum \Delta(\rho W_z^2 A_z)$  in Fig. 11.a. shows higher magnitude than SW case over the axial front part of the CT slots. This result indicates that the flow blowing mechanism energizes the near casing flow in the direction of flow advance. Plots in Fig. 13.b. prove that CT slots reduce the constraint of the net axial force  $\sum \Delta(\rho W_z^2 A_z)$  opposed to the flow advance and located downstream the shock. Further downstream in the channel, curve of  $\sum \Delta(\rho W_z^2 A_z)$  in Fig. 11.a. evolves in positive values over the rear part of CT (blue region in Fig. 13.b). It indicates that flow bleeding mechanism induces net axial force of  $\sum \Delta(\rho W_z^2 A_z) > 0$  acting in opposite direction to the flow advance. Downstream the channel, curve of  $\sum \Delta(\rho W_z^2 A_z)$  evolves similarly to the SW one.

Concerning the CT curve of  $\sum \Delta(\rho W_z W_r A_r)$  in Fig. 11.a., one can notice that flow blowing mechanism creates net axial force  $\sum \Delta(\rho W_z W_r A_r) > 0$  in opposite direction of flow advance. Plots in Fig. 14.b. show that this phenomenon is located at mid-distance in rotor channel (zone C) where flow reinjection is the strongest (Fig. 7). Furthermore, the CT curve indicates a more pronounced effect of the flow bleeding mechanism. In fact, both results in Fig. 11.a. and Fig. 14.b (zone D) prove that blowing effect along the rear part of the CT slots creates a net axial force  $\sum \Delta(\rho W_z W_r A_r) < 0$  directed along the flow advance. Downstream the channel, curve evolves similarly to the SW one.

In order to evaluate the CT mechanisms at lower mass flow rate, Fig. 11.b. compares the cumulative sum curves of both SW and CT configurations for their respective last stable point. One can observe that CT slots permit to return to the same equilibrium of the axial forces than the SW, but to a lower mass flow rate. This last observation further proves the beneficial effect of the CT.

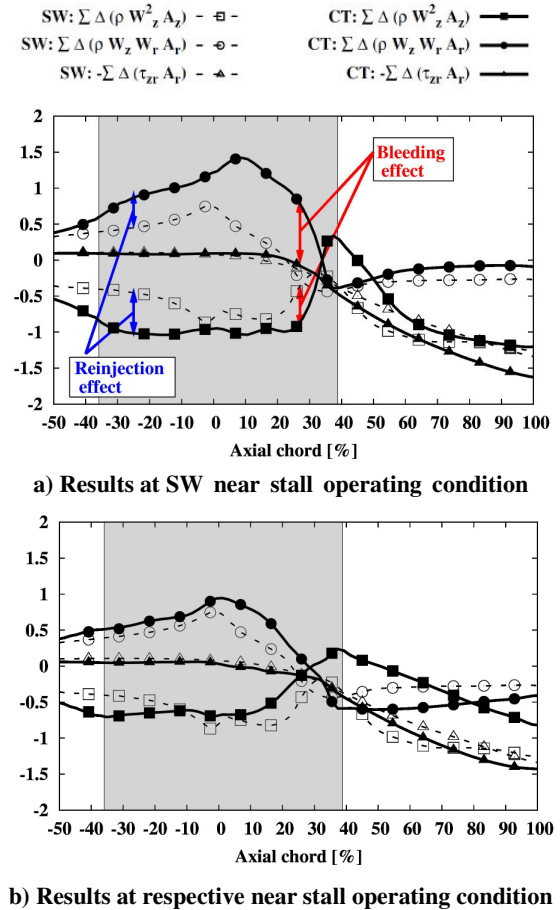
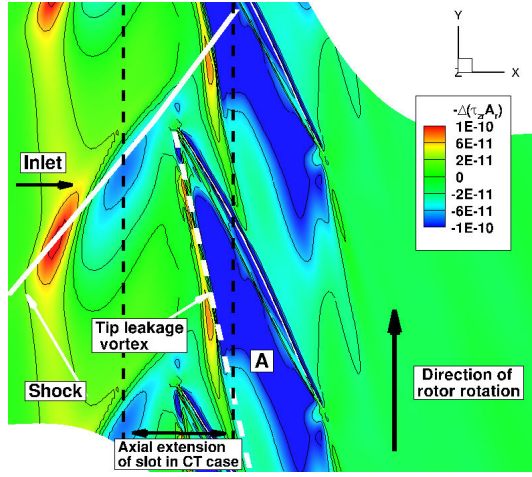
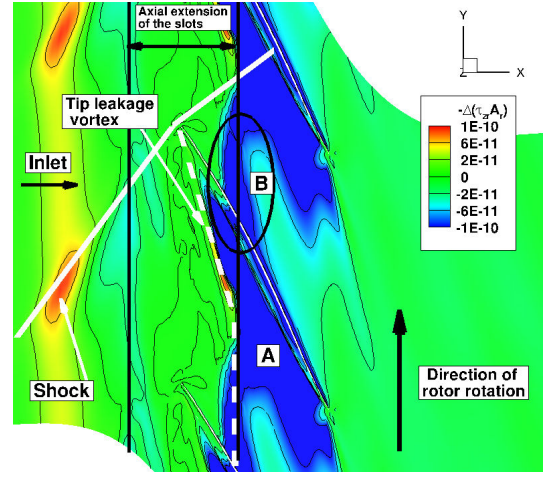


**Fig. 11 Comparison SW vs. CT of the cumulative sum in the axial direction of the main terms of the time-averaged budgets of the axial momentum equation shown in Fig. 9**



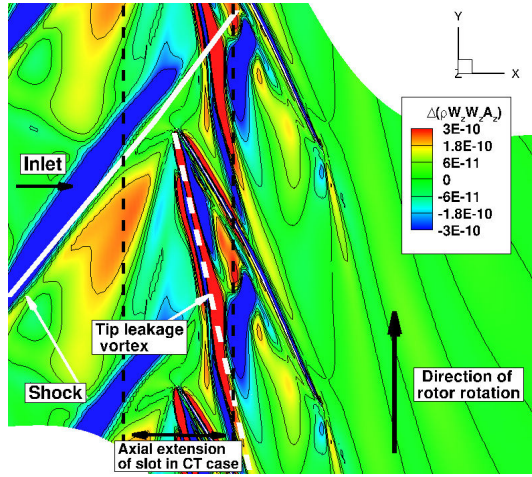


a) SW configuration

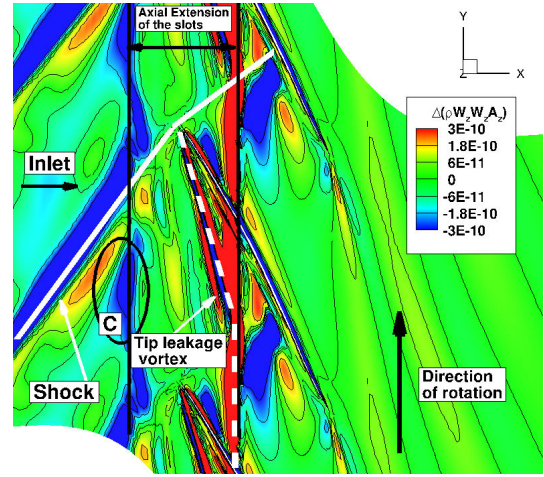


b) CT configuration

Fig. 12 Time-averaged maps of  $-\Delta(\tau_x A_r)$  at  $h/H=97.5\%$  for the SW near stall operating point.

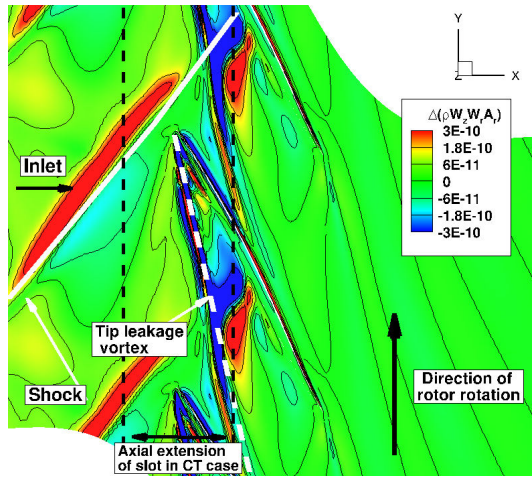


a) SW configuration

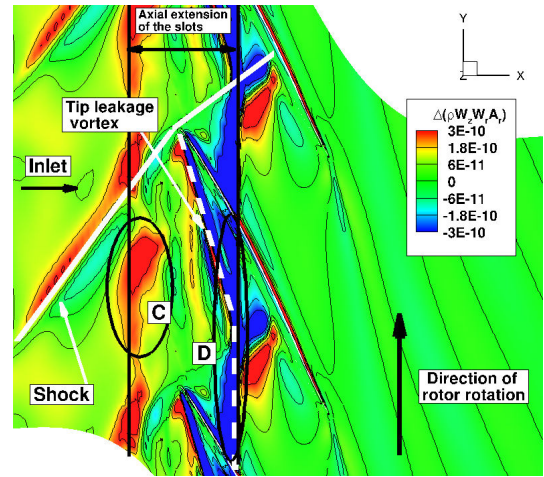


b) CT configuration

Fig. 13 Time-averaged maps of  $\Delta(W_z^2 A_z)$  at  $h/H=97.5\%$  for the SW near stall operating point.



a) SW configuration



b) CT configuration

Fig. 14 Time-averaged maps of  $\Delta(W_z W_r A_r)$  at  $h/H=97.5\%$  for the SW near stall operating point.

## Conclusion

This paper has presented a numerical study of the flows mechanisms induced by slot-type casing treatment in a transonic compressor rotor. Unsteady flow computations have been carried out with the elsA CFD software using an unsteady overset grids method combined with a phase-lagged approach. Numerical results obtained with and without casing treatment have been compared and validated with experimental measurements. Results show that the current slots improve stall margin with penalty in efficiency.

The numerical analysis highlights complex fluid exchanges between slots and the through-flow stream characterized by flow recirculation through the slots from the rear part of the passage to the front and driven by the pressure at casing. The fluid reinjection further upstream of blade leading edge is apparently relevant. This effect enhances the condition near the blade tip by repositioning the tip clearance vortex further towards the trailing edge of the blade passage and delaying the forward movement of tip leakage vortex. This mechanism is assumed to be responsible for the stability enhancement.

In order to get further information about the relevant flow mechanisms, the interaction between slots and the near casing flow has been analyzed through a budget analysis of the unsteady axial momentum equation on a fluid control volume located in the rotor tip region. Results show that flow reinjection provides additional net axial force due to axial transport of axial momentum on the near casing flow. This flow energizing mechanism is assumed to be responsible for delaying the forward movement of tip leakage vortex. At the same time, the bleeding effect creates net axial force due to radial transport of axial momentum that helps to counteract the adverse pressure gradient. Moreover, the bleeding mechanism induces strong shear layers that increase viscous losses, thus explaining the slight decrease of efficiency.

Finally, it is regrettable that the current test case fails to meet expectations in term of analysis of unsteady flow interaction (caused by the large number of slot per rotor blades). However, the current analysis methodology proves its potential to help in the designing of casing treatment.

## Acknowledgement

The authors are grateful to Snecma, SAFRAN Group, for permission to publish results. Special thanks to LMFA and CERFACS-CFD Team for their computational facilities as well as for their availability for discussions concerning numerical methods and physical analysis. The authors are also grateful to the elsA software team (ONERA).

## References

- [1] Greitzer E.M., Nikkanen J.P., Haddad D.E., Mazzawy R.S., Joslyn H.D., (1979), A Fundamental Criterion for the

- Application of Rotor Casing Treatment, *Journal of Fluids Engineering*, Vol. 101, No.3, pp. 237–243.
- [2] Hathaway M.D., (2007), Passive Endwall Treatments for Enhancing Stability. VKI Lecture Series, Belgium.
- [3] Wilke I., Kau H.-P., (2004), A Numerical Investigation of the Flow Mechanisms in a High Pressure Compressor Front Stage With Axial Slots, *ASME Journal of Turbomachinery*, Vol. 126, No.3, pp. 339-349.
- [4] Lin F., Ning F., Liu H., (2008), Aerodynamics of Compressor Casing Treatment Part I: Experiment and Time-Accurate Numerical Simulation. *ASME paper GT2008-51541*.
- [5] Ning F., Xu L., (2008), Aerodynamics of Compressor Casing Treatment Part II: A Quasy-Steady Model for Casing Treatment Flows. *ASME paper GT2008-51542*.
- [6] Lu X., Chu W., Zhu J., Wu Y., (2006), Experimental and Numerical Investigation of a Subsonic Compressor with Bend Skewed Slot Casing Treatment. *ASME paper GT2006-90026*.
- [7] Shabbir A., Adamczyk J.J., (2005), Flow Mechanism for Stall Margin Improvement due to Circumferential Casing Grooves on Axial Compressors, *ASME Journal of Turbomachinery*, Vol. 127, No.4, pp. 708 -718.
- [8] Legras G., Gourdain N., Trebinjac I., (2011), Extended Methodology for Analysing the Flow Mechanisms induced by Casing Treatment in Compressor. In proceedings of the 9<sup>th</sup> European Turbomachinery Conference, Istanbul, Turkey.
- [9] Legras G., Gourdain N., Trebinjac I., Ottavy X., (2011), A nalysis of Unsteadiness on Casing Treatment Mechanisms in an Axial Compressor, *ASME paper GT2011-45806*.
- [10] Castillon L., Legras G. (2011), An Unsteady Overset Grid Method for the Simulation of Compressors with Non Circumferential Casing Treatments, proposed at 20<sup>th</sup> ISABE Conference, Goteborg, Sweden.
- [11] Cambier, L., Veuillot, J.-P., (2008), Status of the Elsa Software for Flow Simulation and Multidisciplinary Applications. In proceeding of 46th AIAA Aerospace Science Meeting and Exhibit, Reno, Nevada, USA, AIAA paper 2008-664.
- [12] Jameson A., Schmidt R. F., Turkel E., (1981), Numerical Solutions of the Euler Equations by Finite Volume Methods Using Runge-Kutta Time Stepping, *AIAA paper* 81-1259.
- [13] Castillon L., Péron S., Benoit C., (2010), Numerical Simulations of Technological Effects Encountered on Turbomachinery Configurations with the Chimera Technique, In proceedings of 27<sup>th</sup> International Congress of the Aeronautical Sciences, Nice, France.
- [14] Wilcox D.C., (1988), Reassessment of the Scale-Determining Equation for Advanced Turbulence Models, *AIAA Journal*, Vol. 26, pp. 1299–1310.